Residual Stress Modeling with Phase Transformation for Wire Arc Additive Manufacturing of B91 Steel

XAVIER JIMENEZ,[1] WEN DONG,[1] SANTANU PAUL,[1]
MICHAEL A. KLECKA,[2] and ALBERT C. TO[1,3]

1.—Department of Mechanical Engineering and Material Sciences, University of Pittsburgh, Pittsburgh, PA, USA. 2.—Raytheon Technologies Research Center, 411 Silver Lane, East Hartford, CT, USA. 3.—e-mail: albertto@pitt.edu

Wire arc additive manufacturing (WAAM) is an energy-efficient manufacturing technique used for near-net-shape production of functional industrial components. However, heat accumulation during deposition and the associated mechanical and metallurgical changes result in complex residual stress profiles across the cross section of the fabricated components. These residual stresses are detrimental to the service life of the components. In this study, sequentially coupled thermomechanical analysis of WAAM B91 steel is conducted to quantify the residual stress variation across the component. The thermomechanical analysis includes a transient heat transfer model and a static stress model that incorporates the transformation-induced plasticity due to martensitic phase transformation. The experimentally calibrated heat transfer model mirrors the temperature variation of the system during the deposition. The results from the stress model are validated via x-ray diffraction measurements, and the numerical results are in good agreement with the experimental data.

INTRODUCTION

Directed energy deposition (DED) is a type of additive manufacturing technique that dispenses and melts a feedstock on top of the workpiece or substrate plate on a layer-by-layer basis. Different energy sources, types of feedstock, and motion systems can be used to obtain different print speeds and qualities. A common DED technique, mostly suited for large parts with medium to low complexity, is wire arc additive manufacturing (WAAM). This technique takes advantage of different welding processes along with metal wire feedstock deposit to create near-net shapes. The most common welding processes are gas metal arc welding (GMAW), gas tungsten arc welding (GTAW), and plasma arc welding (PAW). The welding system can be mounted on a computer numerical control (CNC) table or a six-axis robotic arm to deposit the material based on a three-dimensional (3D) model. The main advantages of WAAM are its high deposition rate and simpler machine setup that allows the creation of large parts, up to several meters long, in a considerable short time when compared with other DED techniques. Low capital investment is also a major benefit of the WAAM process, since the components of a WAAM machine can be derived from open-source equipment from a range of suppliers in the mature welding industry.[1] WAAM does not need the vacuum environment commonly applied in electron beam-based methods to work as required.[2] The use of the electrical arc provides a higher-performance fusion source as opposed to laser-based methods.[3]

The high deposition rate and the intrinsic characteristics of the process make it prone to problems related to residual stress and distortion issues. Because of this, instead of directly printing the part based on a 3D model, an oversized near-net-shape part is deposited and then machined down to the actual tolerances. High-quality production of WAAM parts can only be achieved when the specific challenges of processing materials related to the WAAM process's high-level heat input are addressed.[4] Williams et al.[5] and Ding et al.[6] regarded WAAM's control of high levels of residual

stress and distortion as the primary challenge of heat-related material production. Practical approaches were proposed to alleviate these problems but were limited in scope mainly to the development of strategies for residual stress management.[4] Locally, variations in thermal profiles or differences in thermal history present a material processing challenge, as these can lead to the development of different phases and microstructures within the build, leading to inhomogeneous material properties. As heat dissipation becomes less effective and preheat is introduced from the previous layer, heat can accumulate along the construction direction,[7] leading to a transition zone of microstructural and dimensional variation, which in some cases results in loss of weld bead dimensional control.[8] An interlayer dwelling period is commonly used to minimize the effect of heat accumulation based on a fixed time interval or time connected to reaching a fixed interpass temperature.[9] If these values are specified in such a way that deposition is performed on a surface at sufficiently low temperature, a permanent deposition of the state is possible, identifiable by a constant melt pool (MP) size.

WAAM, like other DED processes, is very similar to multipass welding from a simulation perspective. The transfer of mass and heat between the arc and the workpiece is governed by the MP, which is characterized by complex physical phenomena.[10] Despite some works focusing on MP and arc dynamics simulation,[11] due to unacceptable computational time requirements, such a complex technique cannot be applied at component scale level. WAAM is therefore typically simulated through coupled thermomechanical finite-element analysis (FEA). Using a heat source model, which prescribes a heat generation per unit volume in the MP region, the heat transfer from the arc to the MP is simulated. Most research works employ the heat source developed by Goldak for welding simulations.[12] Montevecchi et al.[10] used a modified Goldak heat source to improve the heat distribution in the filler material. They were able to obtain results generally in good agreement with experimental data without performing a time-consuming tuning process. Ding et al.[6,13] demonstrated that using a steady-state versus a transient heat transfer model provides similar results in a considerable faster time. Ding et al.[14] developed an advanced steady-state thermal analysis model and a 3D thermoelastoplastic transient model. Temperature simulations and predictions of distortion are checked by comparing them with experimental results from thermocouples and laser scanners, while the residual stresses are checked with an ENGIN-X neutron diffraction strain scanner. The stress across the deposited wall is found uniform on the following layers, with very little influence from the preceding layers. Several studies have been published regarding WAAM thermal or mechanical modeling of

different steels, including ER70S-6, ER80S-Nil, A36, and 2209 duplex stainless steel.[9,15–18] In those cases, the residual stress state in the model was comparable to the experimental residual stress.

In metal additive manufacturing that employs a heat source, the deposited material usually undergoes multiple thermal cycles. These thermal cycles result in solid-state phase transformation within the deposit, which is a kind of microstructure evolution that can affect the residual stress and strain distribution of the as-built part. However, this effect differs depending on the material; For example, the influence of the phase transformation on residual stress for Inconel 718 and Inconel 625 has been proved ignorable,[19,20] while it has to be considered for Ti-6Al-4V and HY-130 steel.[20,21] Hu and Zhao found that repeated heating and cooling of P91 steel can result in a solid-state phase transformation that affects the residual stress state of the deposit.[22] Other works found similar results, where lower stress levels were measured at the weld site using x-ray diffraction (XRD) analysis and finite element simulations.[23–27] Yaghi et al.[23,28–30] modeled the welding process of P91 and included the phase transformation effect. To the best of the authors' knowledge, no work exists yet on modeling the WAAM of ER90S-B91, which is the filler material used to join P91 steel. This type of steel is used to fabricate pipes and boilers for the petrochemical and power-generation industries due to its ability to withstand high pressures and high temperatures. As such, P91 is a higher-cost material that can greatly benefit from WAAM through the fabrication of near-net shapes that reduce machining costs and material waste.

In the present study, a thermomechanical FEA method that considers martensitic phase transformation is developed to simulate the WAAM deposition process. The FE model consists of a transient thermal and a steady-state mechanical model that incorporates the effects of phase transformation. For WAAM-processed B91, two types of phase transformations are present in each thermal cycle. When the material is heated up, the microstructure gradually transforms from ferrite to austenite (austenitic transformation). During the cooling process, the austenite is then transformed to martensite (martensitic transformation). Since the former has an insignificant effect on the stress field, in this study, only the martensitic transformation is modeled.[22] The effects of martensitic transformation mainly include (1) volume expansion due to the lattice structure change (from face-centered cubic to body-centered tetragonal system), (2) yield strength change, and (3) transformation-induced plasticity due to atomic migration and reconstruction. The simulation results are validated against experimental data from x-ray powder diffraction analysis obtained on a ER90S-B91 steel deposit. The remainder of this manuscript is organized as follows. WAAM and characterization experiments are

described in "WAAM and Characterization Experiments" section, numerical methods are presented in "Numerical Analysis" section, and results and conclusions are given in "Results and Discussion" section. The numerical methods section covers the thermal model, mechanical model, and phase transformation model.

WAAM AND CHARACTERIZATION EXPERIMENTS

A ten-layer 80-mm-long, 9.6-mm-wide, and 10.8-mm-tall wall was created on a WAAM machine developed by RTRC, where the deposition process was based on plasma arc welding (PAW). The wall (Fig. 1a) was built on the center of an A36 steel substrate by feeding ER90S-B91 wires. Figure 1b shows the experimental setup. The process parameters are presented in Table I. To consider the changes in heat dissipation as the wall grows, parameters for the first two layers are a little different from those for the remaining layers. The deposition path used in the experiment was a simple straight line. Although no preheating or interpass temperature control was used, no observable cracks appeared during or after printing.

Four thermocouples (type K, 0.032″ size, Omega model KMQXL-032U-24) were installed on the substrate close to the deposit area: two on the bottom (TC0, TC1) and two on the top (TC2, TC3), as shown in Fig. 2. The temperature history was recorded with a data-acquisition system.

In addition to the thermocouples, a weld camera was used to monitor MP sizes during deposition. The camera was set up perpendicular to the y–z plane, as shown in Fig. 1b. The camera was attached to the deposition nozzle and captured MP images at the midpoint of the deposition on every layer. The MP width was measured from the bead after deposition was complete. These MP dimensions (length, width, and depth) were used to calibrate the parameters of the Goldak's double ellipsoid model for the heat source as discussed below.

After completing the layer-by-layer deposition, the wall was allowed to cool down to room temperature, and the substrate was released from the clamps. Residual stress measurements were conducted at American Stress Technologies, Inc. by a Stresstech Xstress 3000 Xrobot based on the XRD method. Five locations shown in Fig. 2c were selected for measurement: three on the top substrate (P1, P2, P5) and two on the top deposit (P3, P4). Detailed information about the principle and the procedure of the XRD method can be found in Ref. 31.

NUMERICAL ANALYSIS

Modeling for the WAAM process was achieved through FEA using ANSYS Parametric Design Language (APDL). The analysis consists of a sequentially coupled transient-thermal model and a quasistatic mechanical model. The two models show the same geometry and mesh (Supplementary Fig. S1; Refer to online supplementary material) but different element types (SOLID70 for thermal, SOLID185 for mechanical) and boundary conditions. The number of elements in the model is 73,234, with an average element size of $1 \times 1 \times 1$ cm^3 in the deposit section.

Temperature-dependent properties for the deposit (ER90S-B91 steel) cannot be found in literature, so data were taken for P91 steel. B91 is the fill material used to weld P91 steel, which means these two materials have similar properties. The detailed thermal and mechanical properties for the substrate were obtained from literature.[32] The substrate material properties were compiled from manufacturer data sheets and are available in the Appendix. For a temperature point between the known values, its corresponding material properties were calculated by linear interpolation. Otherwise, for a temperature point beyond the provided range, material properties were evaluated at the closest extreme points. In the simulation, the material behavior was assumed to be perfectly plastic for simplicity.

Thermal Model

The heat transfer in WAAM is governed by the transient heat conduction equation described below:

$$C_p \rho \frac{\mathrm{d}T}{\mathrm{d}t} = \frac{\partial}{\partial x}\left(k\frac{\partial T}{\partial x}\right) + \frac{\partial}{\partial y}\left(k\frac{\partial T}{\partial y}\right) + \frac{\partial}{\partial z}\left(k\frac{\partial T}{\partial z}\right) + Q, \tag{1}$$

where C_p is the heat capacity, ρ is the material density, T is the temperature, k is the thermal conductivity, and Q is the volumetric heat input term.

Goldak's double ellipsoid model,[12] as shown in Supplementary Fig. S2, is employed as the heat source. Its general form is given by

$$Q_i = \frac{6\sqrt{3}P\eta f_i}{a_i bc\pi\sqrt{\pi}}\exp\left(-3\frac{x'^2}{a_i^2} - 3\frac{y'^2}{b^2} - 3\frac{z'^2}{c^2}\right), \tag{2}$$

where Q_i is the power density of the heat source. The subscript $i = 1$ indicates the front part of the heat source, while $i = 2$ indicates the rear part. P is the input power; η is the arc efficiency; a_i and b represent the half-length and half-width of the ellipsoid, respectively; c is the penetration depth; f_i is a scale factor controlling the energy distribution between the front and the rear part of the heat source, $f_1 + f_2 = 2$; and v is the direction of movement of the heat source.

The thermal boundary conditions are shown in Supplementary Fig. S3. Thermal radiation and free heat convection were applied to the outer surface of the deposit with a value of 0.2 W/(m^{2}K) and 10 W/(m^{2}K), respectively. The substrate showed a heat convection coefficient of 10 W/(m^{2}K). The far ends of
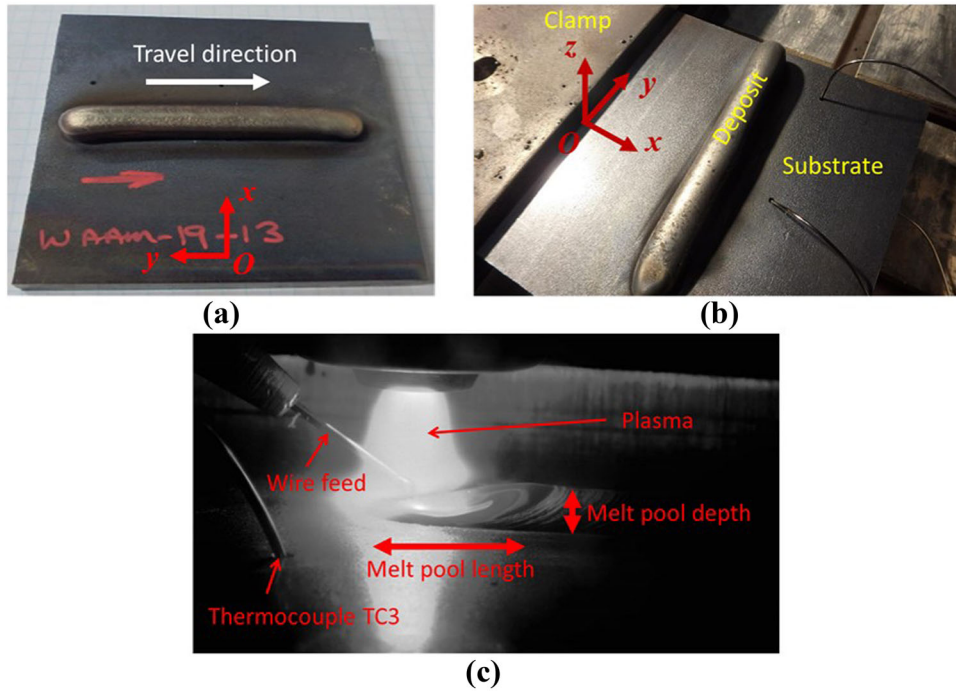
Fig. 1. (a) Manufactured B91 wall, (b) experimental setup, and (c) in situ monitoring with weld camera.

Table I. Process parameters for the WAAM system

Parameter	Value
Average current	Layer 1: 255 A; layer 2: 255 A; layers 3–10: 200 A
Average voltage	Layer 1: 26.9 V; layer 2: 26.9 V, layers 3–10: 23.4 V
Travel speed	Layer 1: 2 mm/s, layer 2: 3.5 mm/s, layer 3–10: 4 mm/s
Wire feed speed	3.1 m/min
Wire diameter	0.889 mm
Delay time after arc ignition	1.5 s
Dwelling time between layers	74.5 s
Plasma gas (argon) flow rate	1 L/min
Shielding gas (argon) flow rate	12 L/min
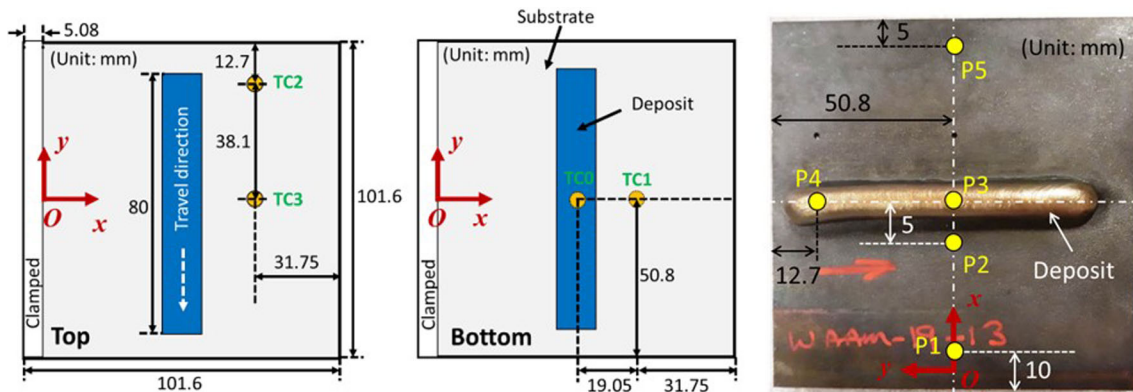
Fig. 2. Thermocouple placement on substrate plate (top); stress measurement points (bottom).

the clamps were fixed at room temperature (20°C) because their temperature is hardly affected by the deposition.

Mechanical Model

After the heat transfer analysis was completed, to further obtain the stress and strain response, a mechanical analysis was conducted where the temperature results were applied as thermal loads in sequential static steps. The governing equation for this thermomechanical analysis can be written as

$$\nabla \cdot \boldsymbol{\sigma} + \rho \boldsymbol{b} = 0, \tag{3}$$

where $\boldsymbol{\sigma}$ is the stress tensor and $\boldsymbol{b}$ is the body force per unit volume.

According to the constitutive law, the stress tensor $\boldsymbol{\sigma}$ is expressed as

$$\boldsymbol{\sigma} = \boldsymbol{C} : \varepsilon_{el}, \tag{4}$$

where $\boldsymbol{C}$ is the fourth order stiffness tensor and ε_{el} is the elastic strain. Total strain ε_{tot} is the sum of elastic strain ε_{el}, plastic strain ε_{pl}, thermal strain ε_{th}, and strain caused by phase transformation ε_{tr}:

$$\varepsilon_{tot} = \varepsilon_{el} + \varepsilon_{pl} + \varepsilon_{th} + \varepsilon_{tr} \tag{5}$$

$$\varepsilon_{th} = \alpha \cdot \Delta T, \tag{6}$$

where α is the coefficient of thermal expansion and ΔT denotes the temperature change.

In steels, cooling rates exceeding $\sim 140°C/s$ cause martensitic transformation, which significantly contributes to the in-process stress evolution.[22,26,32] During the layer-by-layer deposition in an additive manufacturing (AM) process, the cooling rates in the solidified layers far exceeds the critical cooling rate for martensitic transformation in steels. Hence, in this work, we identify the regions for martensitic phase transformation based on the cooling rate and include the following effects of martensitic transformation: (1) volume expansion due to lattice structure change, (2) yield strength change, and (3) transformation-induced plasticity due to atomic migration and reconstruction. Therefore, the total strain increment of the material including these effects is computed as follows:

$$\Delta \varepsilon_{total} = \Delta \varepsilon_{el} + \Delta \varepsilon_{pl} + \Delta \varepsilon_{th} + \Delta \varepsilon_{vol} + \Delta \varepsilon_{trip}, \tag{7}$$

where $\Delta \varepsilon_{el}$, $\Delta \varepsilon_{pl}$, and $\Delta \varepsilon_{th}$ are elastic strain, plastic strain, and thermal strain increment, respectively, and $\Delta \varepsilon_{vol}$ and $\Delta \varepsilon_{trip}$ are strain increments caused by volume expansion and transformation-induced plasticity, respectively.

The strain increment accounting for volume expansion can be calculated by

$$\Delta \varepsilon_{vol} = \varepsilon_0 \Delta f_m (M_f < T < M_s), \tag{8}$$

where $\varepsilon_0 = 3.75 \times 10^{-3}$ is an empirical value[29] and represents the total strain increment of volume

change when all austenite transforms to martensite. Δf_m is the martensitic volume fraction increment and is given by the modified Koistine–Marburger formula[33]:

$$\Delta f_m = 1.141 \left[-0.011 e^{0.011(T-M_s)} \Delta T \right] \quad (M_f < T < M_s), \tag{9}$$

where T is the current material temperature, ΔT is the temperature increment, $M_s = 375°C$[34] is the starting temperature at which the martensitic transformation begins, and $M_f = 185°C$[30] is the ending temperature at which the transformation completes. It assumes that the material contains only austenite when it starts to cool down and that all austenite is transformed to martensite when the temperature reaches M_f. It means that f_m changes monotonically from 0 to 1 in each thermal cycle during the cooling process. As for $\Delta \varepsilon_{trip}$, even though some theories[35,36] and formulas[37,38] explain and calculate transformation-induced plasticity, their applicability is limited due to a lack of data that can only be determined experimentally. Thus, a simplification is adopted here. The influence of the transformation-induced plasticity is considered by reducing the yield strength when the temperature drops below M_s, where the reduction value is 30 MPa.[39] As shown in Fig. 3, ANSYS user material subroutine USERMAT is utilized to calculate and apply the strain increments of $\Delta \varepsilon_{vol}$ and $\Delta \varepsilon_{trip}$ and the change of yield strength. By doing so, the effect of the phase transformation on the stress field is included.

RESULTS AND DISCUSSION

After the transient thermal analysis is finished, temperature histories of the nodes at the thermocouple locations are extracted and compared with the experimental data. Process parameters such as welding efficiency, convective heat transfer coefficients, and emissivity are tuned by trial and error. Generally, on a computer with a 3.2-GHz processor and eight cores, one simulation takes about 8 h. Comparison between the numerical and experimental results after calibration is shown in Fig. 4. For TC0 on the bottom of the substrate, the simulation curve shows good agreement with the experimental curve. Thermocouple TC1 fails during the printing process, and the temperature is only recorded for two layers. For TC2 and TC3 on the top of the substrate, the numerical results can match the temperature trends but fail to capture the peak value for every layer. Since these peaks only appear in the thermocouple measurements on the top surface, a possible explanation is that these peaks are perhaps caused by the plasma gas flowing above the substrate. That is, the dramatic increase or decrease of the temperature in the data does not mean a large amount of heat is absorbed or released

by the substrate. Another explanation could be that the current from the arc is affecting the thermocouple measurements. To summarize, the current heat-transfer model can effectively predict temperature changes and cooling rates during the WAAM process.

The temperature data from the calibrated thermal analysis were imported into the mechanical model to calculate the residual stress field of the sample at room temperature. Two cases are proposed: one without martensitic phase transformation and another with martensitic phase transformation in the deposit. Each case takes approximately 12 h using the same computer as in the thermal analysis. The von Mises stress distribution is shown in Fig. 5 for both cases. As shown in Fig. 5a, the von Mises stress of almost the entire surface of the deposit reaches the yield strength after printing except for its extremities, when phase transformation is not included. However, the von Mises stress on the surface of the deposit is reduced significantly when the phase transformation is considered, as shown in Fig. 5b.

The temperature and stress history at the P3 location is plotted for both models in Fig. 6. For the model without phase transformation (Fig. 6a), once the part is completed and the cool-down period starts, an increase in stress appears that levels off very closely to the yield for the material (415 MPa). For the case with phase transformation (Fig. 6b), a similar trend of increasing stress appears, but once the transformation temperature is reached, the stress is reduced.

Table II presents a comparison between the experimental and numerical values in terms of von Mises stress at several measurement points. During our initial analysis, it was noted that the XRD analysis results for the deposit were lower than what is commonly seen when printing other materials with WAAM. The team also realized that P5 exhibited an error much higher than the rest of the points and decided to consider it an outlier that would not be part of the discussion. Because of its location, the stress state of P5 might be affected by other phenomena not considered in this study. Without considering phase transformation, the error of the numerical results ranges from −12.6% to +239.0%. Once the effects of the phase transformation are included, the margin of error significantly narrows down to +1.9% to +21.0%. Furthermore, all the simulation results now fall within the XRD standard deviation, and hence, it can be concluded that the sequentially coupled thermomechanical model by incorporating phase transformation is able to accurately predict the residual stress profile in the part.

The results show that the points located on top or near the deposit exhibit a significantly greater improvement than the points located further away. This effect can be attributed to the fact that the martensitic phase transformation mainly occurs in the deposit and the surrounding heat affected zone, significantly influencing the stress field in those areas.[22] However, the residual stress state in points further away from the deposit might be influenced by other factors, such as clamp conditions, large deflection of the free edge, and uncertainty of material properties, as may be the case for P5.

In WAAM-processed components, postwelding heat treatment (PWHT) is often used to reduce the residual stresses, but it was not performed for this study. Note that PWHT may involve martensite to austenite retransformation, resulting in the formation of retained austenite and martensite phase fractions, which would require more detailed temperature-dependent metallurgical phase calculations, which is beyond the scope of this work.
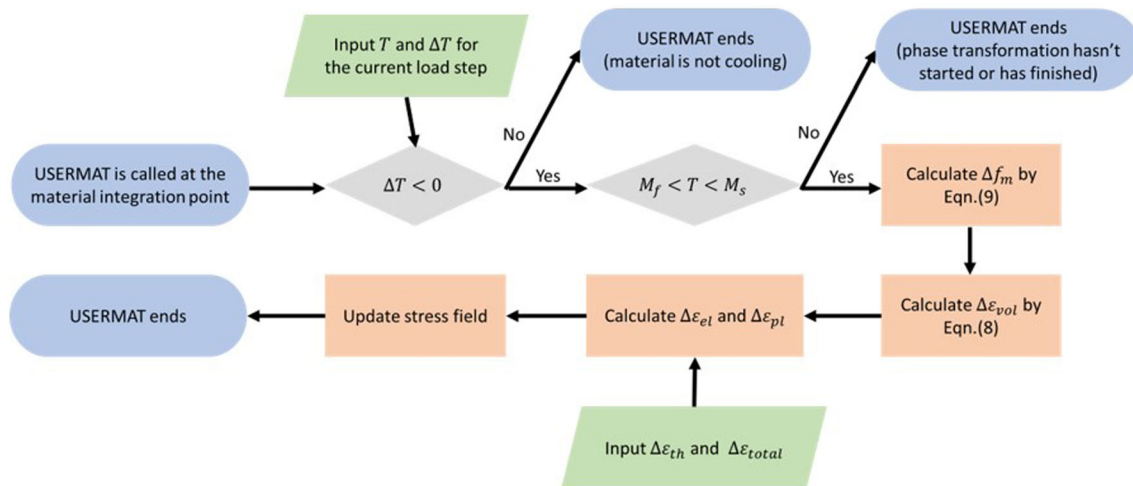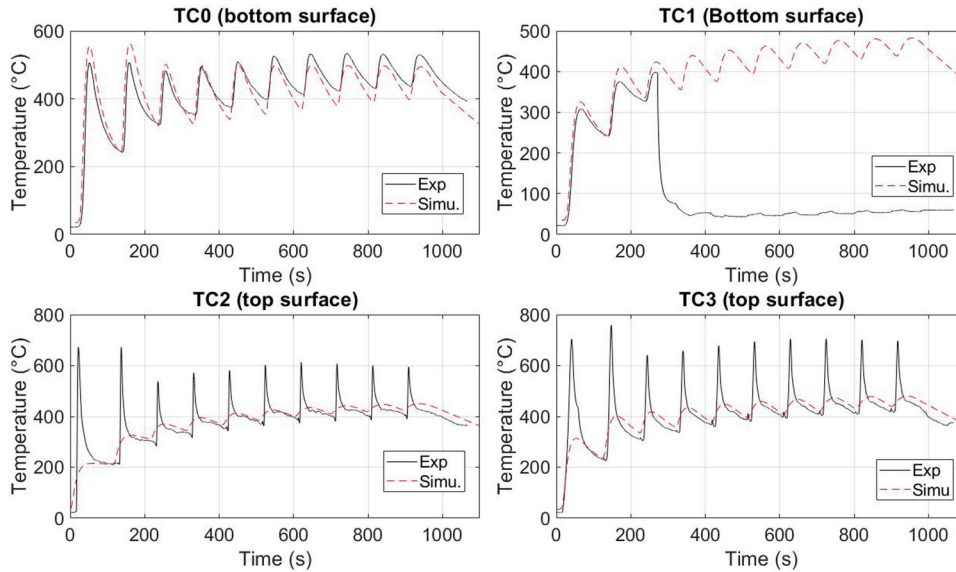

Fig. 3. Flowchart for USERMAT.

Fig. 4. Comparison of temperature histories for thermocouples TC0, TC1, TC2, and TC3.
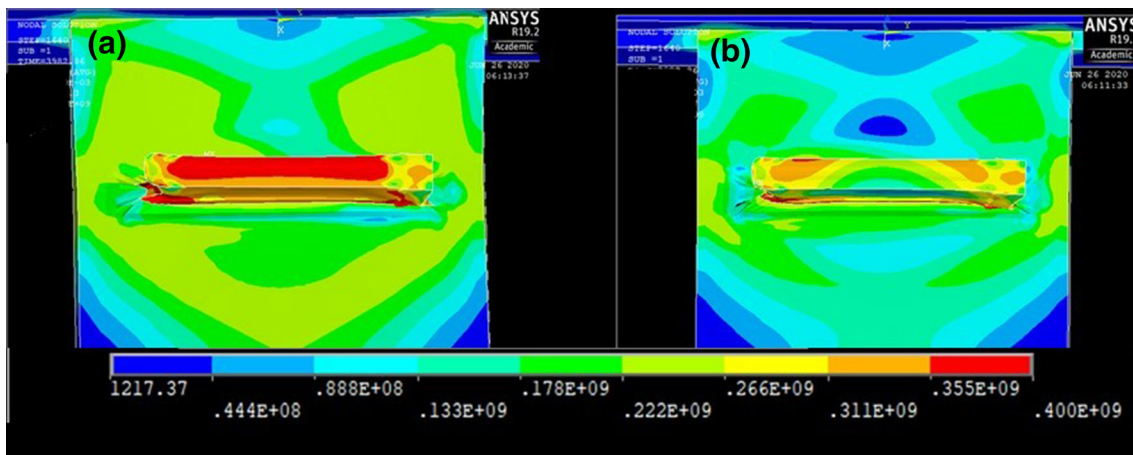

Fig. 5. von Mises stress distribution after printing (a) without and (b) with phase transformation.

CONCLUSIONS

In WAAM, residual stresses and deformations are a big concern because they affect the quality, cost, and accuracy of printing. FEA is a tool that has been successfully used to quantify residual stresses on many WAAM materials. This paper presents two similar FEA models for B91 steel, with one considering the martensitic phase-transformation effect, calibrated using thermocouple data and validated using XRD data. Although most WAAM models in literature do not consider the phase-transformation effect, many welding simulation papers using martensitic steels do. The results show that phase transformation has a major effect on the final stress state of the part, especially in the areas close to the deposit. The error of the simulation versus the XRD measurements was reduced significantly, with the

greatest improvement being $\sim 230\%$. The results are a significant step toward improving the modeling of wire arc manufacturing of martensitic steels, which will allow industry to print higher-quality near-net-shape parts to reduce machining costs and material waste. In terms of computational modeling of residual stresses in AM-processed components, the mechanical modeling approach introduced in this work provides a significant improvement in the computational efficiency of detailed process modeling based on residual stress computation. Note that a detailed process modeling based on residual stress computation requires a mean field-based phase prediction method coupled with thermomechanical analysis. Such a model is restricted to length scales corresponding to a few deposition layers only. In the future, the residual stress distribution for dissimilar
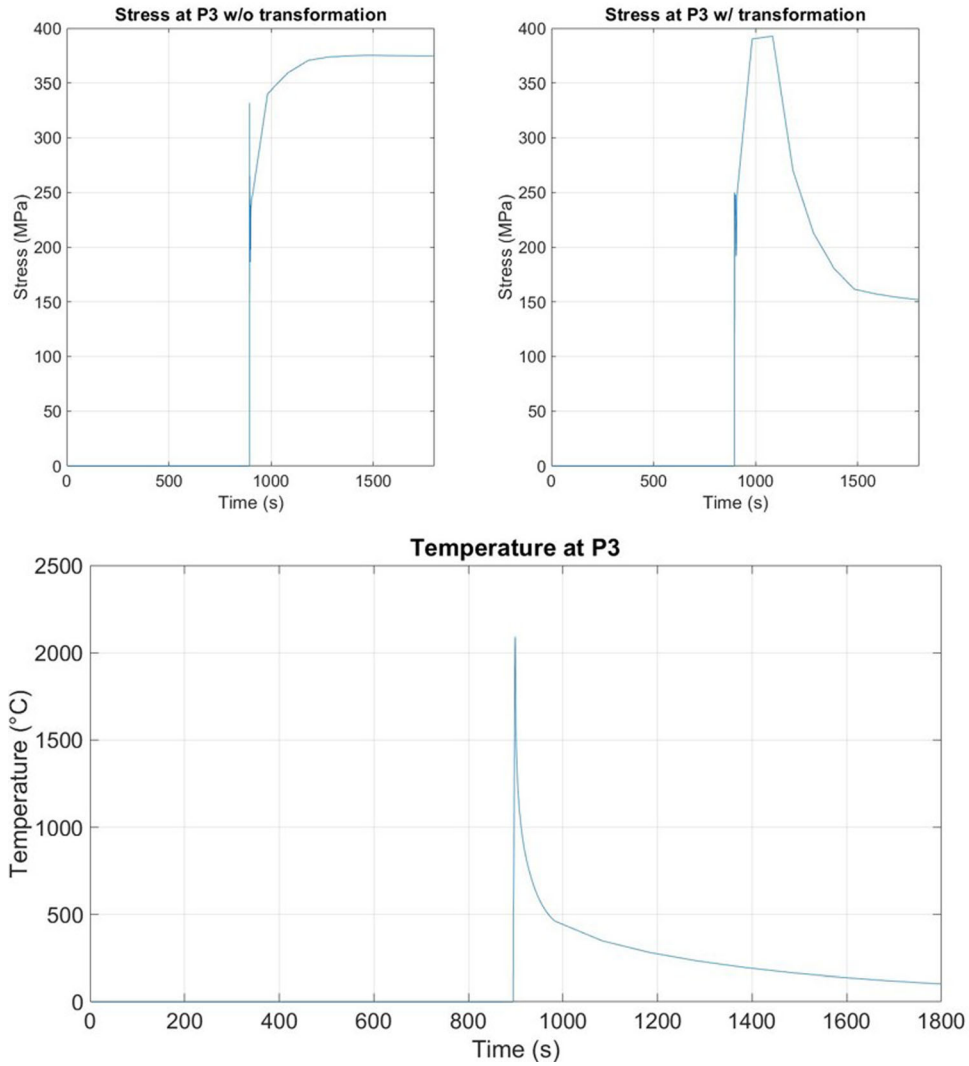
Fig. 6. Temperature and von Mises stress history of point P3: (top) temperature history, (bottom left) without phase transformation, and (bottom right) with phase transformation.

Table II. Comparison of residual stress (von Mises stress) on the substrate and deposit

Location	Index	XRD (MPa)	Simulation without phase transformation		Simulation with phase transformation	
			Residual stress (MPa)	Error with XRD	Residual stress (MPa)	Error with XRD
Substrate	P1	52 ± 5	81	+55.8%	62	+19.2%
(A36)	P2	216 ± 7	190	−12.6%	220	+1.9%
	P5	50 ± 3	219	+338.0%	116	+132.0%
Deposit (B91)	P3	118 ± 44	400	+239.0%	140	+18%
	P4	124 ± 50	181	−46.0%	150	+21.0%

metal deposition will be studied to understand the effect of phase transformations at the interface between dissimilar metal deposits.

CONFLICT OF INTEREST

On behalf of all authors, the corresponding author states that there is no conflict of interest.

ELECTRONIC SUPPLEMENTARY MATERIAL

The online version of this article (https://doi.org/10.1007/s11837-020-04424-w) contains supplementary material, which is available to authorized users.

REFERENCES

1. G.C. Anzalone, C. Zhang, B. Wijnen, P.G. Sanders, and J.M. Pearce, *IEEE Access.* 1, 803 (2013).
2. J.O. Milewski, *Addit. Manuf. Met.* (Springer, 2017), 85–97.
3. M.A. Jackson, A. Van Asten, J.D. Morrow, S. Min, and F.E. Pfefferkorn, fe. *Proc. Manuf.* 5, 989 (2016).
4. C.R. Cunningham, J.M. Flynn, A. Shokrani, V. Dhokia, and S.T. Newman, *Addit. Manuf.* 22, 672 (2018).
5. S.W. Williams, F. Martina, A.C. Addison, J. Ding, G. Pardal, and P. Colegrove, *Mater. Sci. Technol.* 32, 641 (2016).
6. D. Ding, Z. Pan, D. Cuiuri, and H. Li, *Int. J. Adv. Des. Manuf. Technol.* 81, 465 (2015).
7. J.F. Wang, Q.J. Sun, H. Wang, J.P. Liu, and J.C. Feng, *Mater. Sci. Eng. A* 676, 395 (2016).
8. X. Lu, X.F. Zhou, X.L. Xing, L.Y. Shao, Q.X. Yang, and S.Y. Gao, *Int. J. Adv. Des. Manuf. Technol.* 93, 2145 (2017).
9. F. Montevecchi, G. Venturini, N. Grossi, A. Scippa, and G. Campatelli, *Addit. Manuf.* 21, 479 (2018).
10. F. Montevecchi, G. Venturini, A. Scippa, and G. Campatelli, *Proc. CIRP* 55, 109 (2016).
11. J. Hu and H.L. Tsai, *Int. J. Heat Mass Transf.* 50, 833 (2007).
12. J. Goldak, A. Chakravarti, and M. Bibby, *Metall. Trans. B* 15, 299 (1984).
13. J. Ding, P. Colegrove, J. Mehnen, S. Williams, F. Wang, and P.S. Almeida, *Int. J. Adv. Des. Manuf. Technol.* 70, 227 (2014).
14. J. Ding, P. Colegrove, J. Mehnen, S. Ganguly, P.S. Almeida, F. Wang, and S. Williams, *Comput. Mater. Sci.* 50, 3315 (2011).
15. K.P. Prajadhiama, Y.H. Manurung, Z. Minggu, F.H. Pengadau, M. Graf, A. Haelsig, T.E. Adams, and H.L. Choo, *MATEC Web Conf.* 269, 05003 (2019).
16. M. Saadatmand and R. Talemi, *Frattura Integr. Strutt.* 14, 98 (2020).
17. H. Huang, N. Ma, J. Chen, Z. Feng, and H. Murakawa, *Addit. Manuf.*, 101 (2020).
18. F. Hejripour, F. Binesh, M. Hebel, and D.K. Aidun, *J. Mater. Process. Technol.* 272, 58 (2019).
19. X. Liang, L. Cheng, Q. Chen, Q. Yang, and A.C. To, *Addit. Manuf.* 23, 471 (2018).
20. E.R. Denlinger and P. Michaleris, *Addit. Manuf.* 12, 51 (2016).
21. V.J. Papazoglou and K. Masubuchi, *Press. Vessel Technol.* 104, 198 (1982).
22. Z. Hu and J. Zhao, *Mater. Res. Express* 5, 096528 (2018).
23. A.H. Yaghi, T.H. Hyde, A.A. Becker, and W. Sun, *Sci. Technol. Weld. Join.* 16, 232 (2018).
24. A. Kundu, P.J. Bouchard, S. Kumar, K.A. Venkata, J.A. Francis, A. Paradowska, G.K. Dey, and C.E. Truman, *Sci. Technol. Weld. Join.* 18, 70 (2013).
25. S. Paddea, J.A. Francis, A.M. Paradowska, P.J. Bouchard, and I.A. Shibli, *Mater. Sci. Eng. A* 534, 663 (2012).
26. S. Paul, R. Singh, W. Yan, I. Samajdar, A. Paradowska, K. Thool, and M. Reid, *Sci. Rep.* 8, 1 (2018).
27. K.A. Venkata, S. Kumar, H.C. Dey, D.J. Smith, P.J. Bouchard, and C.E. Truman, *Proc. Eng.* 86, 223 (2014).
28. A.H. Yaghi, T.H. Hyde, A.A. Becker, and W. Sun, *J. Strain Anal. Eng. Des.* 43, 275 (2008).
29. A.H. Yaghi, T.H. Hyde, A.A. Becker, and W. Sun, *Proc. Inst. Mech. Eng. Part L* 221, 213 (2007).
30. A.H. Yaghi, T.H. Hyde, A.A. Becker, W. Sun, G. Hilson, S. Simandjuntak, P.E.J. Flewitt, M.J. Pavier, and D.J. Smith, *J. Press. Vessel Technol.* 132, 011206 (2010).
31. H.T. Tran, Q. Chen, J. Mohan, and A.C. To, *Addit. Manuf.* 32, 101 (2020).
32. H. Eisazadeh, A. Achuthan, J.A. Goldak, and D.K. Aidun, *J. Mater. Process. Technol.* 222, 344 (2015).
33. D.P. Koisstinen, *Acta Metal.* 7, 59 (1959).
34. L. BlaRes, A. Balogh, and W. Irmer, *Weld. Res.* 319, 233 (2001).
35. C.L. Magee and H.W. Paxton, *T. Carnegie Inst. Technol.* (1966).
36. G.W. Greenwood and R.H. Johnson, *Proc. R. Soc. London A* 283, 403 (1965).
37. J.-B. Leblond, *Int. J. Plast.* 5, 573 (1989).
38. J.-B. Leblond, J. Devaux, and J.C. Devaux, *Int. J. Plast.* 5, 551 (1989).
39. C.T. Karlsson, *Eng. Comp.* 38, 227 (1989).